Drag Reduction with a Spanwise Synthetic Jet on a Generic Road Vehicle

Cédric Leclerc[1] and Azeddine Kourta[2]
[1]Renault, 1, avenue du Golf, 78288 GUYANCOURT, FRANCE
[2]PRISME, Université d'Orléans, 8 rue Léonard de Vinci,
45072 ORLEANS Cedex 2, FRANCE

Abstract
The aerodynamic drag reduction of a simplified vehicle, by means of a synthetic jet, is studied numerically. The numerical simulations are based on the Lattice-Boltzmann method. The synthetic jet is implemented in an open-loop control strategy. The performances of the actuator are evaluated in 3D configurations. Moreover, an extensive parametric study, by varying independently the momentum coefficient, the jet frequency and its location, is performed and discussed in details. Prior to the flow control analysis, the main features of the reference case, i.e. without control, are deeply investigated in terms of topology and dynamics as well. The optimal parameters of the synthetic jet are found and their influences onto the flow are emphasized by spectral analysis the near-wake unsteadiness and the complex interaction between the actuation and the flow. The drag reduction reaches 5% and 13% when the actuator is set upstream and downstream the corner between the roof and the rear window, respectively.

Keywords: Active control; Synthetic jet; Drag reduction; Lattice Boltzmann Method; Ahmed body

NOMENCLATURE

C_P	=	Static pressure loss coefficient
C_{Pi}	=	Total pressure loss coefficient
C_d	=	Drag coefficient ($C_d = \frac{F_d}{0.5\rho U_\infty^2 S}$, S=$H_A l_A$)
C_{d0}	=	Drag coefficient in non controlled case
ΔC_d	=	Drag reduction (%) ($\Delta C_d = 100\frac{C_{d0} - C_d}{C_{d0}}$)
C_μ	=	Momentum coefficient
d	=	width of the synthetic jet
D	=	Rear window separation
$\overline{e}$	=	Lattice Boltzmann kinetic energy
F_w^+	=	Reduced frequency (f_j/f_w)
f_i	=	Lattice Boltzmann distribution function
f_j	=	Synthetic jet frequency
f_w	=	Natural body wake frequency
F_d	=	Drag force (component of the aerodynamic force along x)
H_A	=	Height of the simplified car geometry
h	=	Height of the underbody flow
k	=	Turbulent kinetic energy
L_A	=	Length of the simplified car geometry
l_A	=	Width of the simplified car geometry
$\vec{n}$	=	normal vector
P, P_i	=	Static pressure and total pressure
P_{io}	=	Reference total pressure
Q	=	Torus vortex (annulus structure)

Q_1, Q_2	=	Upper and lower sides of torus vortex Q
Re	=	Reynolds number
S_t	=	Strouhal number
T_1, T_2	=	Longitudinal vortices
U_∞	=	Free stream velocity
$\bar{U}_j$	=	Synthetic jet velocity
u^+	=	Friction velocity
U_{max}	=	Jet amplitude
(V_x,V_y,V_z)	=	*x, y, z* components of the local velocity
V_i	=	Lattice Boltzmann distribution velocity
w	=	Length of the synthetic jet
$(\omega_x,\omega_y,\omega_z)$	=	*X, Y, Z* components of the local vorticity
(x,y,z)	=	Coordinate system related to the simplified car geometry
y^+	=	Wall coordinate
α	=	Tilted angle
λ_{Q1}, λ_{Q2}	=	distance from the base of the Ahmed body to the upper and lower sides of torus vortex Q
ρ,ρ_0	=	Density and reference density
v	=	Kinematic viscosity
v_t	=	Turbulent eddy viscosity
ε	=	Turbulent dissipation
τ_p	=	Wall shear stress
ω_j	=	Synthetic jet pulsation
$\bar{\omega}_i$	=	Lattice Boltzmann collision term
Ω_i	=	Mesh sub-domain
Ω_f	=	Computational flow domain
Ω_A	=	Geometry of Ahmed body
$\sum_i$	=	Wall Ahmed body surfaces

I. INTRODUCTION

New international standards aimed at limiting greenhouse gas emissions are prompting the automobile industry to develop innovative and efficient systems able to reduce fuel consumption on future vehicles. The development of optimal aerodynamic control appears as one of the most promising ways for achieving this goal. Most road vehicles are essentially bluff bodies [1] meaning that their aerodynamic drag is dominated by the pressure drag due to the flow separation at the rear end of the body. Furthermore, it is well established that the flow field in the wake of the vehicle body is highly three-dimensional and unsteady. Instead of using real vehicles, very simplified (generic) vehicle models, reproducing the main features of real vehicles, are used in laboratories. Using this approach, one expects to identify and isolate the more relevant physical parameters of the flow and the impact of the actuation. Ahmed et al. [2] introduced a generic car model whose wake topology depends strongly on the rear slant angle.

Flow separation control is of major interest in fundamental fluid dynamics as well as in various engineering applications [3-14]. Numerous techniques have been explored to control the flow separation either by preventing it or by reducing its effects. These methods range from the use of passive devices to the use of active control devices either steady or unsteady (synthetic jets, acoustic excitation) [15-19]. Among the various strategies employed in aerodynamic control, conventional passive control techniques, consisting in modifying the shape of the vehicle to reduce the aerodynamic drag, appears as the easiest to implement [20-23]. Unfortunately, this simplicity is also the main drawback of such devices which are often irrelevant when the flow configuration changes. Indeed, the modification of the shape that produces better aerodynamic properties requires a thorough understanding of turbulent flows around vehicles. Current research efforts are now focusing on active flow control techniques as an alternative to conventional design-modification solutions. Flow control on road vehicle geometry, especially on an Ahmed body has been studied in the past by experimental and numerical means. Passive control has been performed experimentally by using vertical splitter plates [20], vortex generators [21], a deflector [22]. Active flow control has also been performed experimentally by using plasma actuator [24], continuous suction or blowing from a slot, jets,

continuous [2527] or pulsed jets [28]. Numerical studies have been done by using statistical turbulence modeling or LES [29-31].

In this paper, the flow around simplified car geometry is controlled by means of a synthetic jet. In areas where the shape of the vehicle naturally generates flow separation, the fluid (air) surrounding the vehicle is periodically sucked in and then blown to form a jet and locally generate vortices in an autonomous manner (no additional air supply). At the actuator orifice exit, the average flowrate during a given cycle is zero, while non-zero net momentum is generated during the blowing and suction phases [9, 32-33]. The efficiency of this control mechanism has already been demonstrated on continuously curved geometries such as cylinders [12, 13] or wing profiles [8, 9].

The present work addresses the efficiency of a synthetic jet to control the flow on a simple geometry featuring the edges, breaks, low-radius connection curves and the separation regions occurring at the roof, quarter panel, rear window and at the base of an automobile vehicle. We focus only in the rear part. The goal is to control rear window flow separation. A preliminary study of a 2D configuration is performed on the simplified geometry of an automobile vehicle representing the roof, a rear window tilted at 25°, a base and a smooth underbody. Then 3D simulations are conducted and compared with the 2D computations. In both cases, an extensive parametric study of the controlled flow is carried out in order to determine the optimal control parameters.

The paper is organized as follows. The numerical method and the geometries are depicted in Section 2. The numerical results are presented and discussed in Section 3. In particular, the aerodynamic drag coefficient (C_d) and the topology of the mean flow in the wake are analyzed as functions of two characteristic parameters of the synthetic jet, namely its momentum coefficient (C_μ) and reduced frequency (F^+). The computational results obtained without control are compared to existing experimental and numerical data.

II. NUMERICAL METHOD

II.1-Numerical software

In this study, the numerical simulations are based on a Lattice Boltzmann Method (referred to as LBM in the following) implemented in the commercial software Powerflow. More details about the numerical method used here can be found in previous publications [19, 34, 35]. The basics of the LBM consists in building simplified kinetic models that incorporate the essential physics of microscopic processes such that the macroscopic-averaged properties are in accordance with the appropriate macroscopic equations. The basic premise for these simplified kinetic-type methods to be used for simulating macroscopic fluid flows stands in the fact that the macroscopic fluid dynamics result from the collective behavior of many microscopic particles in the system and that the macroscopic dynamics are not sensitive to the underlying details as is the case in microscopic physics [19, 20]. The fluid particles are distributed on a Cartesian lattice of computation nodes [19]. For each lattice node, a distribution function $[f_i]_{i=1...N}$ is associated with a discrete velocity distribution $[\vec{V}_i]_{i=1...N}$ representing N possible velocities of motion. The kinetic energy is given by $\bar{e} = \frac{1}{2}\sum_{i=1}^{N} V_i^2$. One particle, initially located on one node, can either stay at this node (energy level 0: $\bar{e} = 0$), move toward an adjacent node in horizontal or vertical plane (energy level 1: $\bar{e} = 1$) or move to a farther node (energy level 2: $\bar{e} = 2$). As a consequence, the model gives 34 possible combinations and is therefore referred to as the 34 velocities model (2 possibilities for level 0, 18 for level 1 and 14 for level 2). More details concerning the algorithm can be found in [19,3438].

The macroscopic variables (density ρ, momentum density ρu and internal energy ρe_{int}) are defined as particle velocity moments of the distribution function f_i along the i^{th} direction.

$$\begin{cases} \rho(\vec{r},t) = \sum_{i=1}^{N} f_i(\vec{r},t) \\ \rho(\vec{r},t)\vec{u}(\vec{r},t) = \sum_{i=1}^{N} \vec{V}_i f_i(\vec{r},t) \\ \rho(\vec{r},t)e_{\text{int}}(\vec{r},t) = \sum_{i=1}^{N} \left|\vec{V}_i\right|^2 f_i(\vec{r},t) - \frac{1}{2}\rho(\vec{r},t)\left|\vec{u}(\vec{r},t)\right|^2 \end{cases} \quad (1)$$

The objective of the simulation is therefore to determine the distribution $[f_i]_{i=1\ldots N}$ of particles for each node on the lattice. This distribution is obtained according to the Boltzmann equation (Eq. (2)) governing the particle dynamics at the microscopic (mesoscopic) level [18-19, 36-39]:

$\frac{\partial f_i}{\partial t} + \underbrace{\vec{V} \cdot \overrightarrow{grad(f_i)}}_{\text{advection}} = \underbrace{\bar{\omega}_i}_{\text{collision}}$ That can be writing in discontinuous form as:

$$f_i\left(\vec{r} + \vec{V}_i\Delta t, t + \Delta t\right) - f_i(\vec{r}, t) = \bar{\omega}_i(\vec{r}, t) \tag{2}$$

where $\bar{\omega}_i$ is the collision operator which represents the rate of variation of f_i resulting from the collision whereas Δt and $V_i\Delta t$ are the time and space increments, respectively. The RHS depends on Δt but to simplify equation (2) for farther developments, this time increment is set equal to 1.

In the Boltzmann equation (2), the distribution function f_i evolves in 2 phases. During the first phase, i.e. the propagation phase, each particle is considered as an independent entity. N possibilities of motion, associated with N velocities $[V_i]_{i=1\ldots N}$, are attributed to each node on the lattice (left-hand term of equation (2)). In the second phase, a collision model is used to describe the impacts that occur between the particles and to redistribute the particles on the lattice (right-hand term of equation (2)). This type of simple description of the particles dynamic, with the help of the Chapman-Enskog development [19], leads to Navier Stokes equations solutions.

At this level, the problem consists in determining a collision model $[\bar{\omega}_i]_{i=1\ldots N}$. Bhatnagar, Gross and Krook [38] noticed, that the main effect of the collision term is to bring the velocity distribution function closer to the equilibrium distribution. The representation selected for this term is then that proposed by Bhatnagar et al (BGK) [38], in which the collision is associated with a relaxation of the excited state of the particles before impact and a state of equilibrium after the impact. The simplest way of approximating the collision term is by using a single relaxation time approximation. The collision term is then obtained according to the equation (3):

$$\bar{\omega}_i(\vec{r}, t) = \frac{f_i^{eq}(\vec{r}, t) - f_i(\vec{r}, t)}{\tau_r} \tag{3}$$

in which τ_r is the relaxation time and $\vec{f}_i^{eq}$ the distribution of particles in a state of equilibrium at the node defined by the position $\vec{r}$ at date t.

In the BGK representation [38], the collision model is then completely characterized by the state of equilibrium $\vec{f}_i^{eq}(\vec{r},t)$ and by the relaxation constant τ_r (equation (3)). These 2 parameters are indicated by Chen et al. [39]:

$$\begin{cases} f_i^{eq} = \rho\omega_i \left[1 + \dfrac{\vec{V}_i \cdot \vec{u}}{T} + \dfrac{\left(\vec{V}_i \cdot \vec{u}\right)^2}{2T^2} - \dfrac{|\vec{u}|^2}{2T} + \dfrac{\left(\vec{V}_i \cdot \vec{u}\right)^3}{6T^3} - \dfrac{\vec{V}_i \cdot \vec{u}}{2T^2}|\vec{u}|^2\right] \\ \tau_r = \Delta t\left(\dfrac{v\Delta t}{T|\Delta\vec{r}|} + \dfrac{1}{2}\right) \end{cases} \tag{4}$$

in which T represents the temperature, v viscosity and ω_i the weighting coefficients associated with each i^{th} direction. All variables are in non dimensional form [19]. The non dimensional temperature T is constant and equals to 0.42. The weighting coefficient ω_i is related to T by (5):

$$\begin{cases} \omega_1 = 3T^2 - 3T + 1 \\ \omega_2 = \dfrac{T}{2}(2 - 3T) \\ \omega_3 = \dfrac{T}{24}(3T - 1) \end{cases} \tag{5}$$

The general algorithm for the LBM is thus defined in 4 stages. The first consists in propagating the distribution function in time t+1 (left-hand term of Eq. (2)). In the second stage, the collisions between the particles are modelled (right-hand term of Eq. (2)). The collision operator $[\bar{\omega}_i]_{i=1\ldots N}$ is then defined by equations (3) and (4) applied to time t-1. The third stage consists in determining the associated values of density and density momentum according to Eq. (1). Finally, the fourth stage consists in initiating iteration on the basis of the macroscopic values determined in the third stage (Eq. (4)) [39].

Such as all numerical space-time methods, the LBM is unable to resolve the entire range of turbulence scales. Consequently, the computation code requires a turbulence model to be used. In this study, the RNG k-ε model, originally developed by Yakhot et al. [40], has been chosen. The transport equations of kinetic energy and dissipation applied by the model are resolved on the same lattice as the Boltzmann equations. The numerical simulations are performed using a second-order discretization diagram in space (Lax-Wendroff finite difference model), coupled with a time-explicit integration diagram [41]. Close to the wall, a specific velocity law is applied to limit the computational workload [41]. The velocity is then described by a logarithmic law. This law is applied for the wall coordinate y^+ between 30 and 300.

II.2-Numerical simulation protocol

The numerical simulations reported in this paper were conducted on a simplified vehicle geometry initially proposed by Ahmed et al. [2]. Note that the computation is exclusively focused on the rear part. The geometry is the same as the one previously computed [19, 34-36]. The consequence of this limitation is that the boundary layer thicknesses on roof and sides can be not exactly reproduced. However, as stated by Ahmed et al. [2, 42, 43], the interference between the rear end and the fore body flow is weak; this may be a consequence of the relatively long midsection. This statement has been confirmed by Krajnovic and Davidson [44, 45] with LES calculations. In computations done on the complete body, along the roof after the leading edge separation and reattachment, a classical boundary layer is found. Hence, to obtain the main important characteristics at the rear body (the separation and longitudinal vortices), the length of the present body is fixed in such way that the boundary layer thickness at the end of the roof be equivalent to the one of the complete Ahmed body.

Recently, Conan et al. [46] performed oil visualization on the front of Ahmed body when changing the rear slant angle from 10° to 40°. They observed that this experiment does not show any important difference while changing the rear part. This again confirms the fact that the interference between the front and the rear part is weak. They also observed the separation in the front part of the body even though not observed by Ahmed and confirm that this separation is linked to the definition of the model itself. This detachment can be removed by gluing a strip of sand paper before the separation line, the roughness forcing the transition to turbulent and avoiding the flow separation. In this case, the flow is fully turbulent and the drag calculated is changed in consequence.

The geometry is defined by its length (L_A=1.044 m), its width (l_A=0.389 m) and its height (H_A=0.288 m). In this configuration, the rear window with a length of 0.222 m, is tilted at an angle of 25° with respect to the horizontal (figure 1). Finally, the lower part is positioned at $0.17H_A$ from the floor of the numerical wind tunnel. The geometry is located in a rectangular numerical box of length, width and height equal to $31L_A$, $20L_A$ and $10H_A$ respectively. These dimensions ensure that there is no interaction between the boundary conditions, imposed at the limit of the computational domain, and the development of the near-wake flow (see [18]). The outlet condition, downstream from the geometry and on the upper part, is a free flow condition [18] on pressure and velocity. The flow is convected from left to right and a uniform velocity U_∞ =40m.s^{-1} is applied to the left-hand surface of the computational domain (Dirichlet velocity condition). The Reynolds number, based on the inlet velocity and the length LA of the geometry, is Re =2.8×10^6. Finally, symmetry conditions are applied on the side surfaces of the computational domain [19]. The origin O of the coordinate system is located at the bottom of the base (figure 1).

The present study is part of various control strategy on the same geometry. The mesh dependent has been already done on previous works [18-19, 34, 36, 43]. Here, the same mesh is used. The simulation volume is subdivided into parallelepiped domains. Inside each domain, the volume mesh is Cartesian, uniform and the resolution is halved as it moves away from the surface. Each block Ω_k is associated with a resolution level δx_k, defined by: $\delta x_k = 2^k . \delta x_0$, in which δx_0 represents the most refined resolution, i.e. the size of an elementary computation cube in the block having the highest resolution.

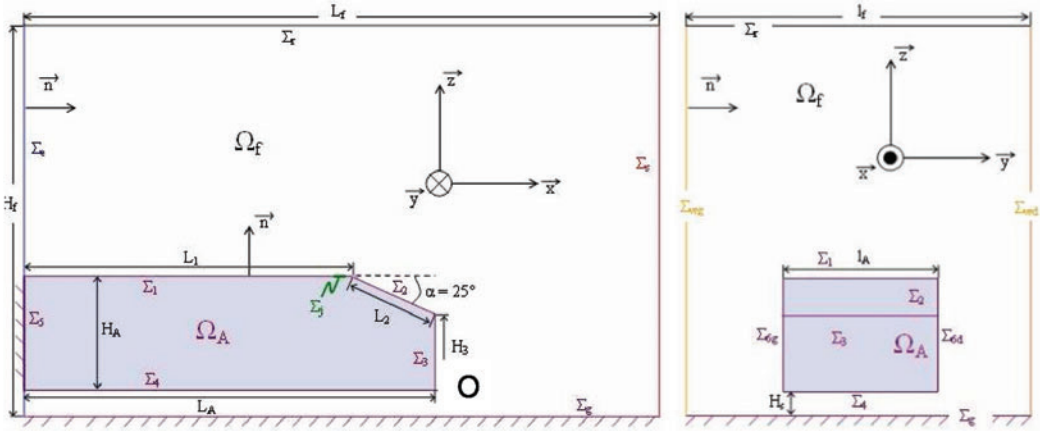

Figure 1. Simplified model and computational domain

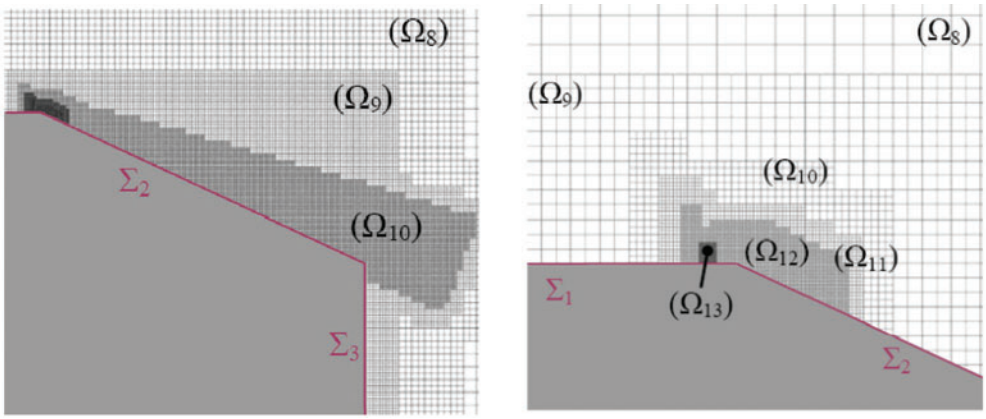

Figure 2. mesh structure

In the present case, 13 levels of blocks $[(\Omega_i)_{i=0,12}]$ have been created: the fourth most refined levels are located in areas generating high gradient and flow separations, close to the geometry (fig. 2). For a 2D computations, the length of the sub-domain Ω_{12} is equal to 1.2×10^{-4} m with the theoretical thickness of the boundary layer at the end of the roof equals to Re = 2.0×10^{-2} m and the first computation node, at the end of the roof, is located at y^+=30 (with $y^+ = y.\frac{u^+}{v}$ and $\tau_p = \rho u^{+2}$, v the viscosity of the fluid and u^+ the friction velocity). The mesh size is 1.8×10^5 with 1.4×10^4 distributed around the geometry.

For the 3D case, the length of the sub-domain Ω_{12} is equal to 2.5×10^{-4} m and the first computation node, at the end of the roof, is located at $y^+ \sim 40$. The mesh size is 1.5×10^7 with 1.3×10^7 distributed around the geometry.

To increase the number of elements around the synthetic jet position a sub-domain Ω_{13} is added (see figure 2). This treatment is applied at each different position of the actuator. The length of this sub-domain is equal to 10^{-4} m in a 2D and 1.25×10^{-4} m in a 3D case.

From one block to the next one (Ω_i to Ω_{i+1}), the mesh density is divided by 2. The finer mesh is used near the wall and in the region with high gradient. So moving from the wall to the free stream, the mesh density decreases. The time step Δt has to respect the CFL criterion. This criterion is based on the smallest cell size $|\overrightarrow{\Delta x_s}|$. The CFL number is kept constant all over the computational domain thus the time step is proportional to the cell size. So the time step is doubled from one block to the next one. This procedure increases the convergence. The convergence is based on the drag coefficient error. The convergence is attempted when the relative error is smaller than 1%. For the convergence 10^5 iterations are used and for the flow analysis 2.0×10^5 added iterations are performed. The smallest time step is equal to 6.8×10^{-7} s.

The boundary condition related to the synthetic jet is imposed at the wall of Ahmed body by prescribing the wall normal velocity component:

$$\vec{U}\cdot\vec{n}(\vec{X},t)=\overline{U_j}(\vec{X},t)=U_{\max}\cos(\omega_j t)\cos\left(\frac{\pi x_j}{d}\right)$$

Where U_{max} is the amplitude and ω_j is the pulsation.
The control momentum coefficient is defined by:

$$C_\mu=\frac{U_{\max}^2 dw}{4U_\infty^2 H_A l_A}$$

With d is the width and w the length of the synthetic jet slot.

For 2D computations, the actuator position is located 10^{-3} m upstream from the top of rear window. For 3D, two actuator positions have been used 10^{-3} m respectively upstream and downstream from the top of the rear window. The width d is the same in 2d and 3D and is equal to 5.0×10^{-4} m. In 3D case, the actuator length corresponds to 95% of the width of the rear window. Five mesh points are used to describe the width of the slot. This simplified vision of the problem does not take into account the resonance phenomena generated during the interaction between the flow and the actuator cavity.

III. COMPUTATIONAL RESULTS

III.1-Preliminary results: 2D computations

The goal of this work is to control separation on the rear window. In this part we would like to isolate this separation from longitudinal vortices. These last structures are due to a 3D effect. So, a 2D computation allows to have only the rear window separation. Moreover, these 2D computations can help experiments and 3D computations to understand the separate effects of separation and longitudinal vortices separately and their interaction.

The spanwise vorticity component (ω_y) computed in the wake near the base, plotted in figure 3, reveals the presence of the von Karman vortices (T_1 and T_2). Another small structure (T_3) appears at the end of the rear window. The characteristic resolved frequencies of the fluid flow in the near wake are determined by analyzing the pressure signals collected at positions P_1 and P_2, respectively located 10^{-2} m downstream from both the bottom and the top of the base. The dominant frequencies (f_1= 18 Hz and f_2=12 Hz respectively for positions P1 and P2) are associated respectively to the top and the bottom vortex shedding. The corresponding Strouhal numbers are $S_{t1}=f_1H_A/U_1=0.13$ and $S_{t2}=f_2H_A/U_2=0.14$ (where U_1 the free velocity at the top side $U_{\infty 1}$=40 m/s, and U2 the free velocity at the bottom side $U_{\infty 2}$=24 m/s. U_2 is smaller than U_1 (used only in 2D) to take into account the under body effect. Besides the main vortex shedding frequencies f_1 and f_2, the power density spectrum computed from the drag coefficient exhibits a noticeable peak at the frequency combination f_1-f_2. This specific frequency results from an interaction between the vortex shedding released from the bottom and the top of the base. This non-linear coupling phenomenon induces an excitation which might be assimilated to a low frequency flapping. The energy loss generated by the structures evolving from the von Karman instability is related to a total pressure $C_{pi}\left(C_{pi}=\frac{P_{i0}-P_i}{\rho U_\infty^2/2}\right)$ for the mean flow [46]. The evolution of C_{pi} shows an important total pressure loss in the wake. Values greater than 1.75 are detected near the vortex center of the structure T_2. These high values are the consequence of the vortex shedding in the wake. At the rear window ($\sum_2$) T_1 and T_3 vortices provide the formation of two recirculation zones where the total pressure loss coefficients are approximately equal to 1.3.

In this 2D case, as in one case studied in 3D, the actuator slot is set on the roof, slightly upstream from the rear window (-1 mm). The jet is normal to the wall. For a fixed frequency (F_w^+=1, f_w=140 Hz), the momentum coefficient effect is studied by varying C_μ from 6.8×10^{-6} to 6.8×10^{-4} . Figure (4) shows the drag reduction evolution as a function of C_μ. For the values of C_μ ranging between 1.6×10^{-5} and 3.5×10^{-5} this reduction varies between 16% and 19% (region A). For higher values of C_μ, it decreases and reaches a value around 14% (region B). This evolution is in good agreement with previous results obtained on airfoil (Seifert et al. [8], Glezer et al. [9]).

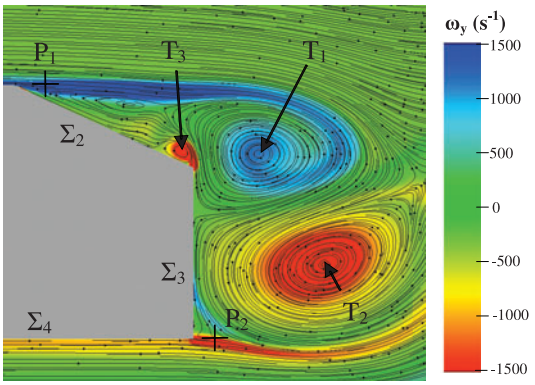

Figure 3. typical snapshot of vorticity distribution

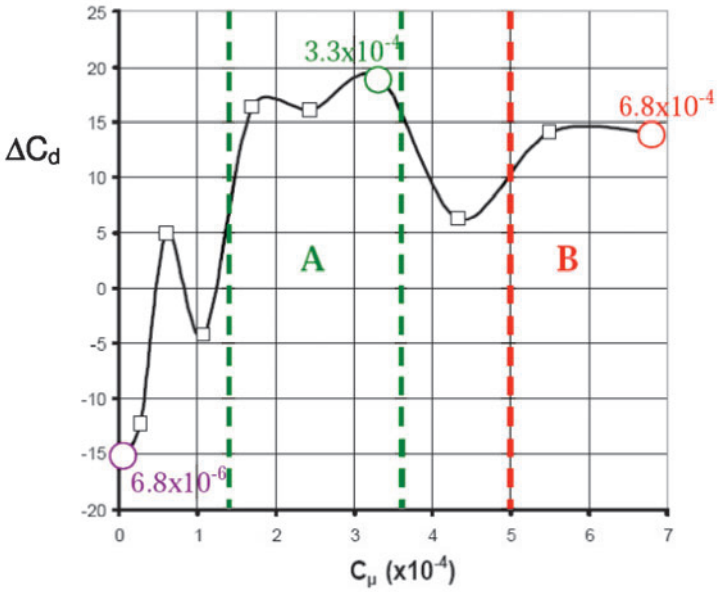

Figure 4. Drag reduction (%) variations with Cμ for F_w^+ =1

At the base, the pressure coefficient $C_p \left(C_p = \frac{P_0 - P}{\rho U_\infty^2 / 2} \right)$ increases with increasing C_μ even though no relevant differences are visible between the reference case and the flow control case with the lowest C_μ. It is worth noting that the contribution of the base to the drag is higher than that of the rear window. This results in a reduction of the global drag by 18% in the case of C_μ=3.3×10^{-4} and by 14% in the case of C_μ=6.8×10^{-4}

It is well known that the synthetic jet frequency is a key parameter for the control. The effect of this parameter has been evaluated by varying the reduced frequency F_w^+, while keeping Cμ unchanged (equal to 1.1 × 10^{-4}). The maximum drag reduction (28%) is achieved for F_w^+=0.7 (see Fig. 5). The drag reduction sharply decreases around this reduced frequency and then increases again until approximately 10% beyond F_w^+=2.

From this analysis, a conclusion can be drawn in the optimal case (F_w^+=0.7 and C_μ=2.4×10^{-4}). The shedding of both vortex structures T1 and T2 are driven by the synthetic jet frequency. These structures move separately along horizontal lines without interacting.

III.2-Three dimensional computations

In this part, the properties of the flow computed around the Ahmed body, with and without control, is investigated and discussed in details by using 3D computations.

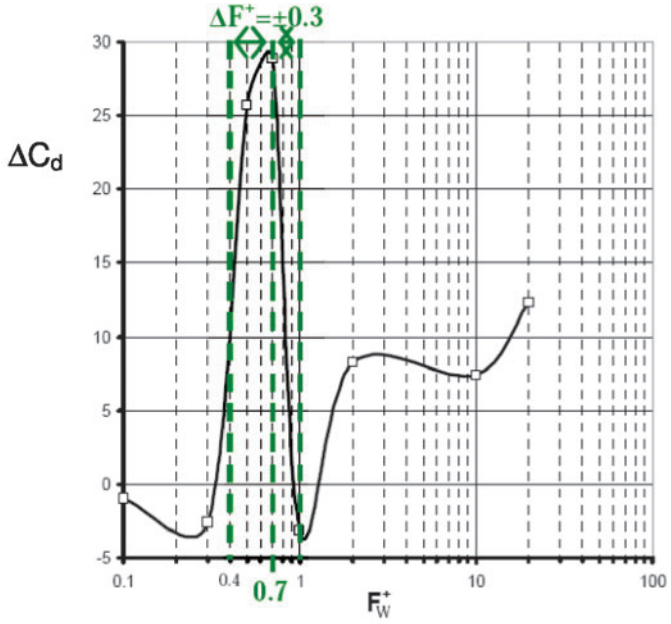

Figure 5. Drag reduction (%) function of F_w^+ (C_μ=1.1×10^{-4})

III.2.1-3D flow without control

III.2.1.a-Mean Flow characterization in the near wake

As reported by Krajnovic [44, 45], the topology of the flow remains approximately the same for Reynolds numbers higher than 10^4. In this study, two velocities have been chosen 25 m/s and 40 m/s corresponding respectively to Reynolds numbers equal to 1.7×10^6 and 2.8×10^6 . The iso-values of the total pressure, displayed in Fig. 6, clearly illustrate the main features of the flow topology in the near-wake. The separation zone on the rear window (D), the longitudinal vortices (T_1 and T_2) and the torus structure (Q) on the base are well identified. Furthermore, one can observe the interaction between the separation zone and the structure at the base. This topology is in agreement with experimental results reported by Ahmed. The streamlines show that the rear window is only connected to the flow coming from the roof. The flow separates at the corner between the roof and the rear window until it reattaches on the second part of the rear window. At the bottom of the rear window, streamlines converge to a symmetric plane. Then, one more time, the flow separates at the base producing, consequently, a torus structure. This structure has different forms at the bottom due to the ground effect. Finally, at each side, a longitudinal vortex is formed.

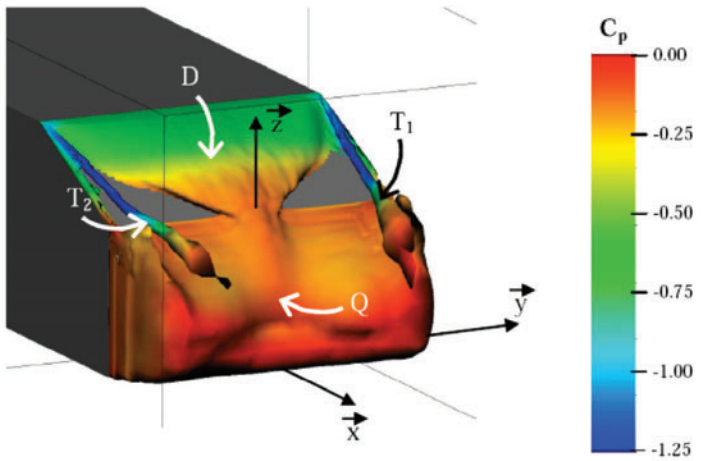

Figure 6. Iso-pressure coefficient (C_{pi}=1, *Re* =2.8×10^6)

This analysis shows that the main characteristics of the mean flow are well predicted, especially the separated bubble zone. In Figs. 7 and 8, the normalized profiles of mean velocity and turbulent kinetic energy are compared to experimental measurements obtained from both LDA [47] and PIV [48] in the plane of symmetry. This comparison is given for both Reynolds numbers. The numerical velocity profiles agree fairly well with the experimental data (figure 7), more especially with the PIV measurements. One can observe that the mean velocity is noticeably underestimated on the rear window in comparison to the LDA measurements. It is worth noting that this discrepancy is also visible between LDA and PIV data. It is therefore reasonable to think that the LDA underestimates the separation bubble on the rear window. Furthermore, the good agreement between experimental and numerical results shows clearly that the front part does not affect significantly the flow on the rear part. The turbulent kinetic energy is underestimated as with other statistical turbulence model (figure 8). However, this underestimation does not affect the main topology of the flow. The comparison between LDA and PIV measurements shows that the turbulent kinetic energy computed from the PIV measurements is smaller than that obtained from the LDA in the half top part of the rear window, whilst it is higher in the second part. Moreover, the location of the maximum of kinetic energy from the wall is higher with PIV and computation than with LDA measurement. These results confirm that the size of the separation zone is underestimated by the LDA system.

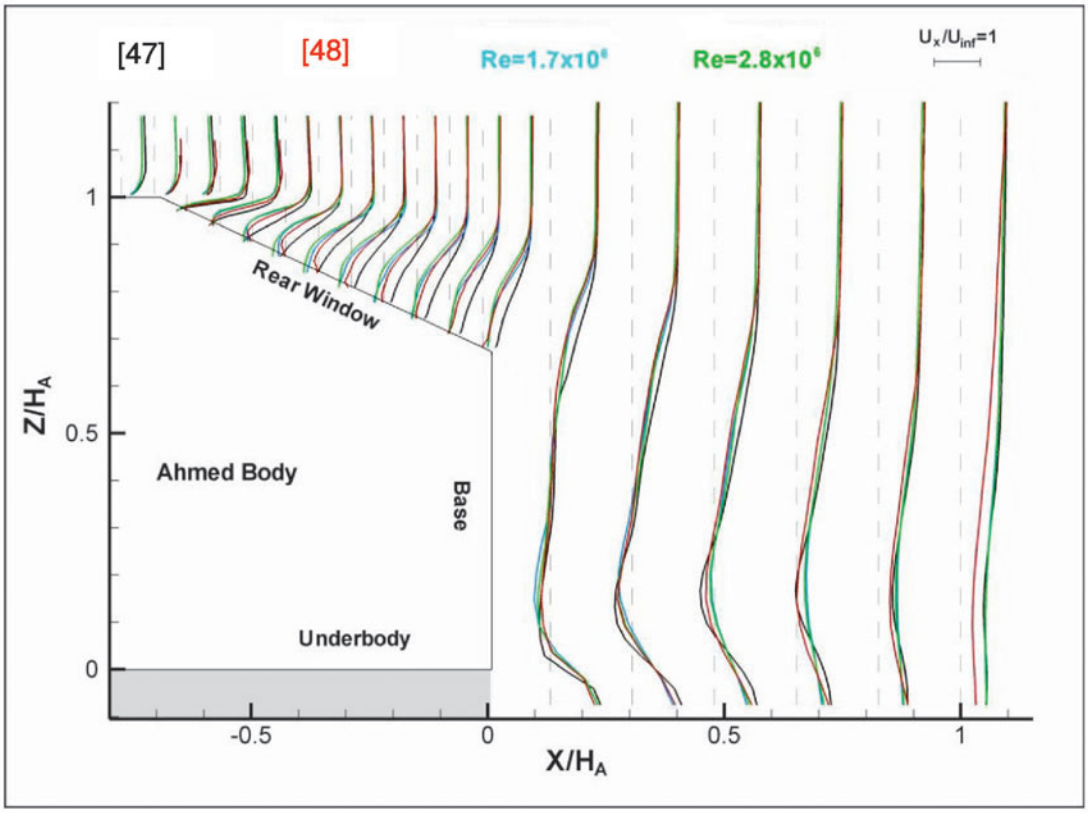

Figure 7. Velocity profiles

The effect of the longitudinal vortices can be evaluated by comparing the 2D simulations with the mid-plane of the 3D simulations. The pressure losses, shown in Fig. 9 for both simulations, clearly evidence the differences in the topology of the wakes. On the rear window, the energy losses C_{pi} are higher in 3D than in 2D (1.6 and 1.3 respectively), while at the base, these energy losses are smaller for the 3D computations (1.75 for the 2D and 1.3 in the 3D case). Note that the pressure loss evolution is intimately correlated with the flow topology. In the 2D simulations, the rear window bubble remains separated up to the base, unlike the 3D case. In the latter, due to the presence of the longitudinal vortices, a reattachment occurs before the end of the rear window leading to a shorter separation bubble. Moreover, the important energy losses are associated to a von Karman vortex shedding. One can see that in the 2D case, the typical size of the von Karman street is of the same order as the size of the

geometry. Finally, in the 2D case the flow topology near the base is mainly dominated by one large vortex, while in the 3D case, two vortices coexist.

The wall shear stress at the rear window is presented in figure (10) which well illustrates the complexity of the flow. In this graph, our numerical results fairly well compare with experimental visualization. These visualizations confirm the fact that the flow over the rear window is formed by the separated bubble and two longitudinal vortices.

The flow visualization at the base (figure 11) evidences the singularities of the 3D flow revealing that the longitudinal vortices at both end sides perturb the flow at the base.

The drag coefficient Cd obtained in this study are equal to 0.34 for Re = $1.07 \bullet 10^6$ and to 0.32 for Re $=2.8 \bullet 10^6$. These values are 12% higher than those reported in the experimental work by Ahmed et al [2], Lienhart et al [46] and

the numerical simulations by Krajnovic [44, 45] (table 1). This overestimation may be due to the fact that in our case the computation does not include the front part of the Ahmed body. Indeed, the flow analysis in the central plane shows that the separated bubble size is higher in our case, leading therefore

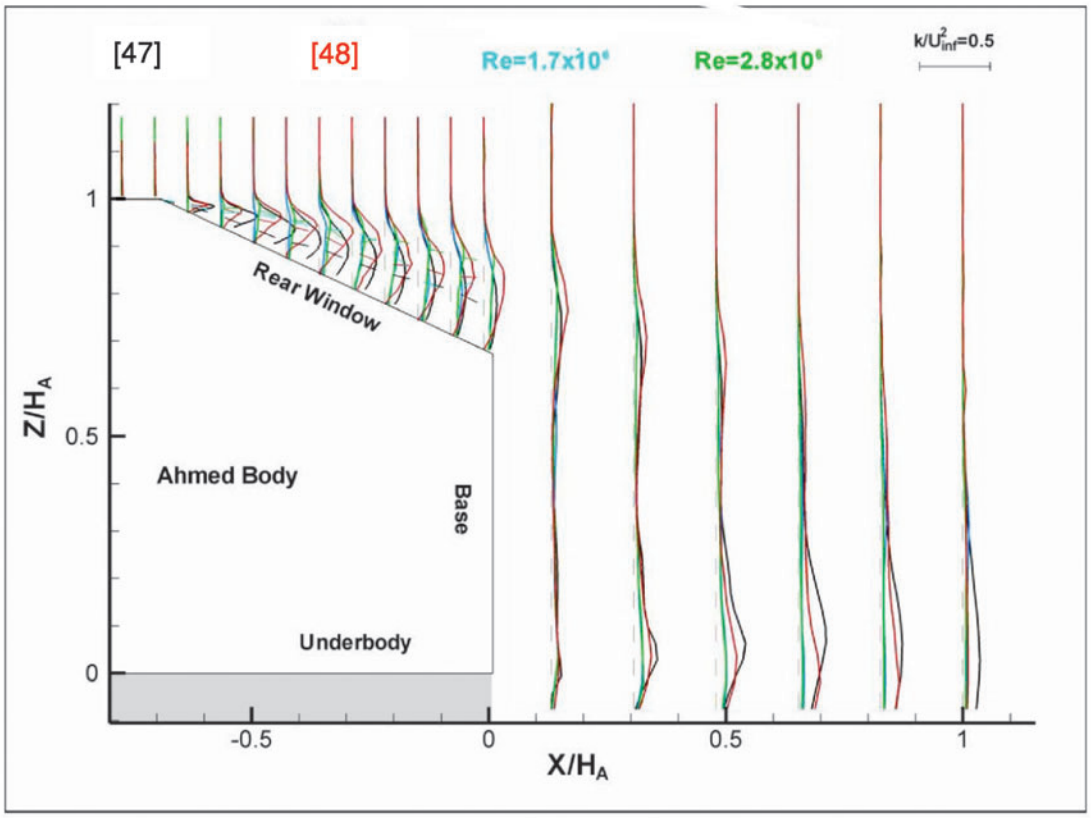

Figure (8): Turbulent kinetic energy profile

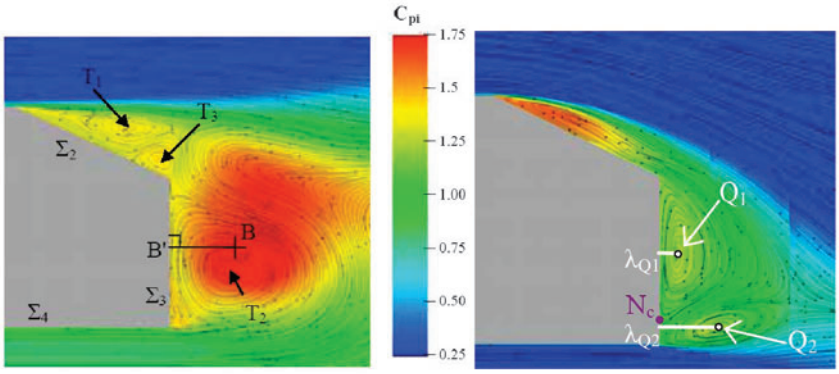

Figure 9. Comparison between 2D (left) and 3D (right) Computations (snapshot of C_{pi})

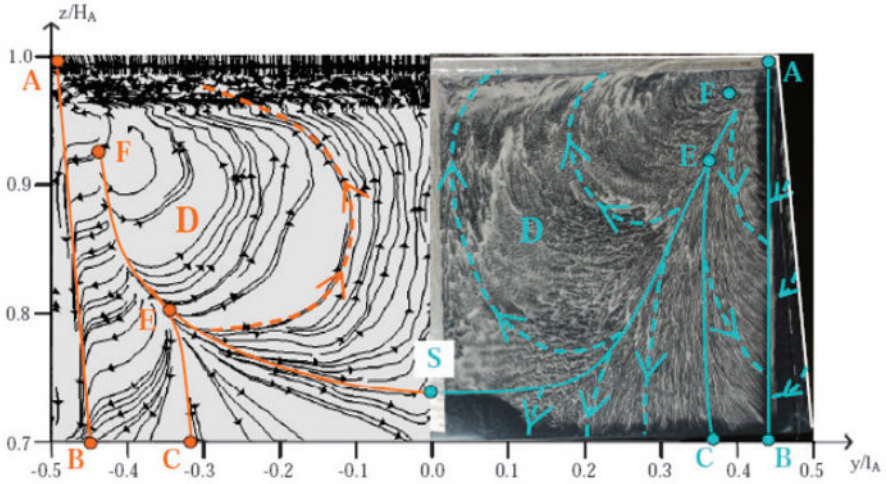

Figure 10. Visualization of surface streaklines along the rear window (left: computation)

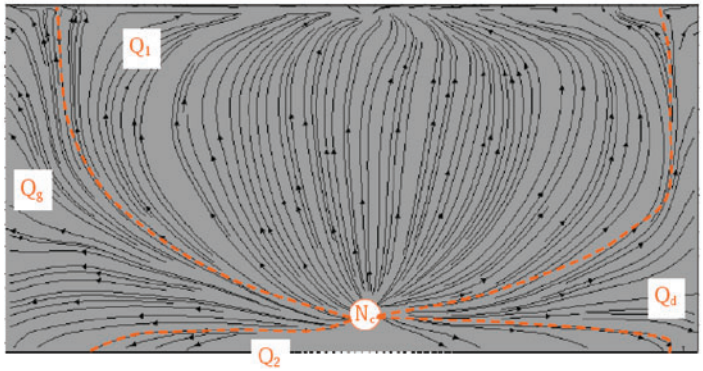

Figure 11. Visualization of surface streaklines along the base

Table 1. Comparison of drag coefficients from various authors

	C_d	Re	α	Ref.
Experiment	0.283	2.8×10^6	25°	[2]
Experiment	0.285	2.8×10^6	25°	[47]
Experiment	0.38→0.32	7.5×10^5→2.8×10^6	30°	[49]
Experiment	0.39	1.0×10^6→1.9×10^6	25°	[47]
Experiment	0.34	4.2×10^6	30°	[44]
Experiment	0.292	2.8×10^6	25°	[46]
Experiment	0.31	2.8×10^6	25°	[18]
Experiment	0.346, 0.317, 0.343, 0.431	0.768×10^6	25°	[50]
Experiment	0.34→0.32	1.07×10^6→2.8×10^6	25°	Present study

to a higher energy loss in the wake and to a diminution of the static pressure on the rear part. This observation can explain the discrepancies between our results and those reported in the literature. Note that, the values of drag obtained in this study are the same as those reported by Vino et al [48] in the case of the rear window with an angle of 30°and Rouméas et al [18] for the same with an angle of 25°. Recent publication [50] reported results obtained on Ahmed body by three different LES methods and one DES method. Compared to the experiment, the drag coefficient was overestimated by 16% by the DES method and by 6%, 15% and 40% by the LES methods. One of the main purposes of this study consists in simulating properly the dynamics of vortices in order to evaluate the control effect onto the flow topology and its dynamics as well.

III.2.1.b-Unsteady flow characteristics

In order to distinguish the unsteady contribution of the actuator from the flow, it is essential to first investigate the flow dynamics without control. Figure (12) shows the power spectral density (PSD) of the longitudinal velocity component, computed at several locations, versus Strouhal number $S_t = \frac{fH_A}{U_\infty}$. The PSD levels are normalized with the help of $U_\infty{}^2$. The velocity time series is cut into 10 equi-length signals with 85% overlapping. So the frequency resolution is equal to 17 Hz. Near the bottom side, one peak is visible at S_t=0.4, in agreement with the observations by Vino et al [49], Boucinha et al [51] and with computations using LES by Minguez et al [52]. In this numerical study, the plotted power spectra density of u shows high pick at S_t=0.4 downstream of the base. This frequency corresponds to the shedding of vortices Q_2 coming from the bottom side of the geometry, i.e. the von Karman instability. This Strouhal number corresponds to the first mode. The PSD obtained at the point downstream of the roof presents one peak at S_t=0.7 as well as the subharmonic S_t=0.3, the first harmonic S_t=1.4 and the second harmonic S_t=2. The presence of these subharmonics shows the coherence of the unsteady phenomenon. The observed peaks correspond to the flapping of the separated bubble on the rear window. Therefore, this spectral analysis reveals the presence of two characteristic dynamics (at S_t=0.4 and 0.7) related to two different unsteady phenomena.

Applying a band-pass filter centered on each characteristic frequency, it has been shown [38] that S_t=0.4 corresponds to a big vortex related to the von Karman instability, while S_t=0.7 corresponds to a smaller structure.

III.2.2-Efficiency of the control on 3D computation

This part focuses on the relevance of drag reduction by means of synthetic jet. For this purpose, the influence of both the C_μ value and the actuator position is investigated. Note that the reduced frequency F^+ is kept constant. To study the C_μ effect the actuator slot is set on the roof, slightly upstream from the rear window (-1 mm). The jet is normal to the wall. The Reynolds number is equal to 2.8×10^6. Three C_μ values have been tested (1.1×10^{-4}, 4.2×10^{-4} and 9.5×10^{-4}) corresponding to U_{max}=20, 40 and 60 m/s. We have observed that the drag coefficient decreases with increasing momentum coefficient. The maximum drag reduction, which reaches 5.2%, has been obtained for $C_\mu = 4.2 \times 10^{-4}$. For higher values of the momentum coefficient, the drag reduction remains unchanged. Let us remind that for the 2D computation a much larger value of drag reduction (28%) has been obtained highlighting the fact that due to the finite size of the body, the surrounding flow is highly 3D. This characteristic has to be carefully taken into account in order to predict properly the flow control efficiency.

III.2.2.a-Effect on vortex structures

The iso-values of energy losses (C_{pi}=1) presented in figure (13) shows the comparison between the cases with and without control. One can see that the actuator modifies essentially the flow over the rear window, which leads to a decrease of the energy loss linked to the separation bubble. This energy loss reduction becomes more pronounced with increasing C_μ.

Without control, values of C_{pi} greater than 1 expands on the overall rear window and interact with the flow over the base. For the lowest C_μ used in this study, the interaction with the base persists, although it is weaker than without control. In that case, the drag reduction is about 3%. For the two highest values of C_μ, the flow evolves in a very similar way. The separation bubble is reduced (70% of the rear window length) and it does not interact any more with the flow downstream of the base. The drag reduction is then found equal to 5%. Moreover, the iso-values associated to the longitudinal vortices are also reduced at their ends further downstream. The synthetic jet reduces the window bubble without annihilating the longitudinal vortices and modifying the torque vortex at the base. An increase of the momentum coefficient creates additional three dimensional structures on the bubble which does not entirely collapse under the control action. The control leads only to the appearance of transverse vortex structures convected along the rear window. The bubble oscillates in phase with the synthetic jet frequency. These results have been obtained also with 2D simulations.

For the longitudinal evolution, an increase of C_μ induces a decrease of circulation bubble on the rear window. The global energy loss increases and is located inside the bubble when the control is on. The C_{pi} values are higher than 1.76 instead of 1.6 in the case without control. Near the base the C_{pi} distribution shows a new organization of the vortices. When the momentum coefficient increases, the

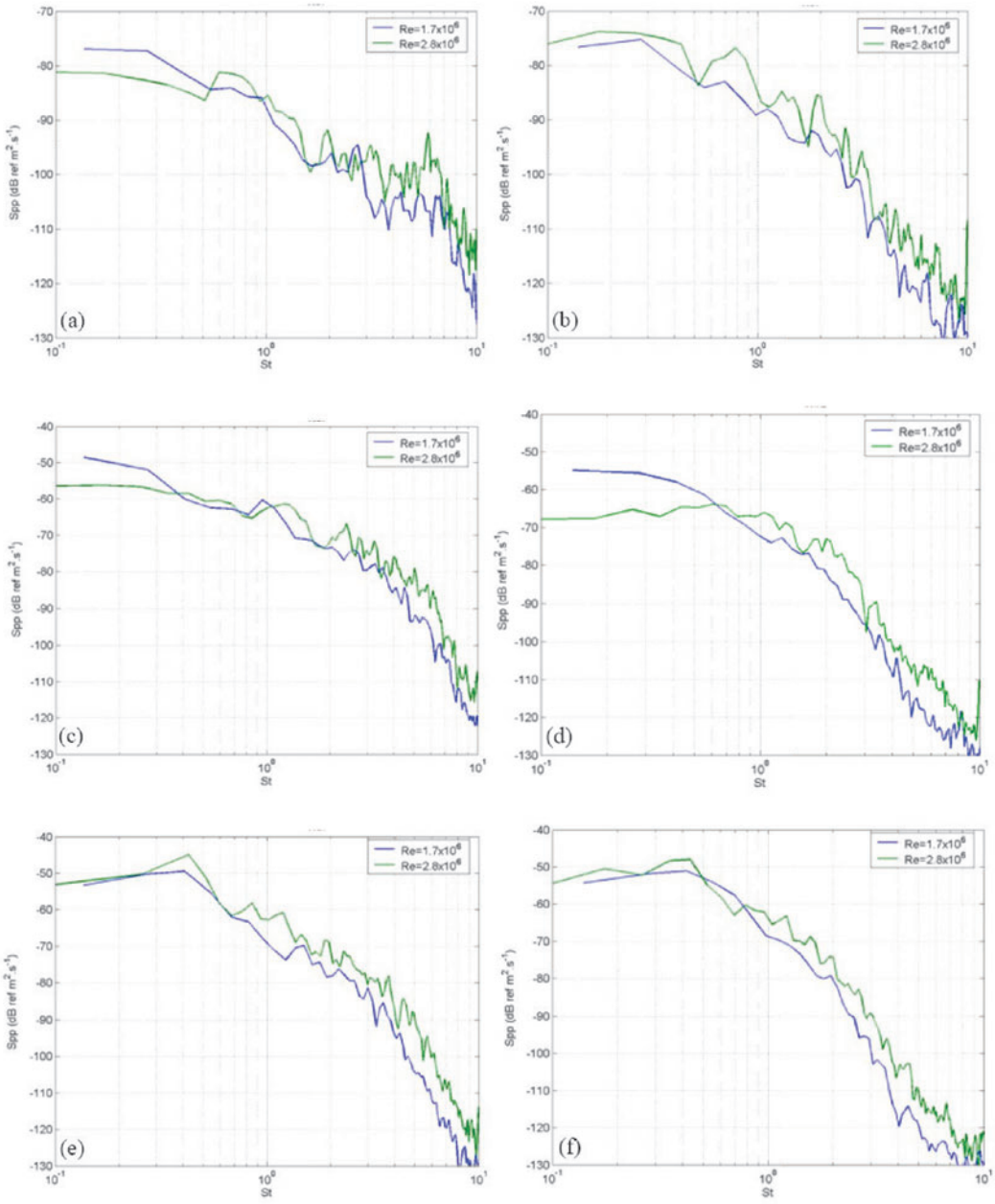

Figure 12. Power spectral density at different wake positions: **a**[x=H_A/2, z=H_A]; **b**[x=H_A, z=H_A]; **c**[x=H_A/2, z= H_A/2]; **d**[x=H_A, z=H_A/2]; **e**[x=H_A/2, z=0]; **f**[x=H_A, z=0]

vortex Q_1 moves downstream and becomes bigger. The distance between the vortex and the base λ_{Q1} is equal to $0.08H_A$ without control, while it becomes equal to $0.16H_A$ for $\lambda_{Q1}=1.1\times10^{-4}$, $0.17H_A$ for $C_\mu=4.2\times10^{-4}$ and $0.18H_A$ for $C_\mu=9.5\times10^{-4}$. For the vortex Q_2 this distance is equal to $0.27H_A$ for $C_\mu=1.1\times10^{-4}$, 0.22 H_A for $C_\mu=4.2\times10^{-4}$, and $0.19H_A$ for $C_\mu=9.5\times10^{-4}$. When the control is on, the vortex structures Q_1 and Q_2 are symmetric. This evolution does not modify the total energy loss. The C_{pi} values at the center of these two vortices still have a value around 1.30 for each value of C_μ tested here. For the highest momentum coefficient value the topology of the flow downstream of the model is symmetric. This behavior has been observed by Rouméas [19] when the flow is attached on the rear window.

The energy loss profile at $x/H_A=0.25$ are plotted in figure (14). Without control, the transversal surface size is equal to $0.95H_A$, 10% reduction of the size of the wake has been reported by Rouméas [19] when suction is applied. With the synthetic jet, the transversal size is increased and is equal to

$1.05H_A$. For the suction actuation, the flow is completely attached. With the synthetic jet, the flow is dynamically attached. 5% drag reduction is obtained with the synthetic jet compared to 15% with the suction actuator.

The pressure evolution at the wall on both the rear window and the rear base has been analyzed. The static pressure coefficient and strain lines are plotted on figure (15). The saddle point S is on $\sum_2$, in the symmetry plane at $x_2=0.80I_2$. When the synthetic jet momentum coefficient C_μ increases, the saddle point moves toward the top of the rear window, in the symmetry plane, confirming, therefore, that the size of the separated bubble decreases. Its length I_d is equal to $0.68I_2$ for $C_\mu=1.1\times10^{-4}$, $0.46I_2$ for $C_\mu=4.2\times10^{-4}$ and $0.42I_2$ for $C_\mu=9.5\times10^{-4}$.

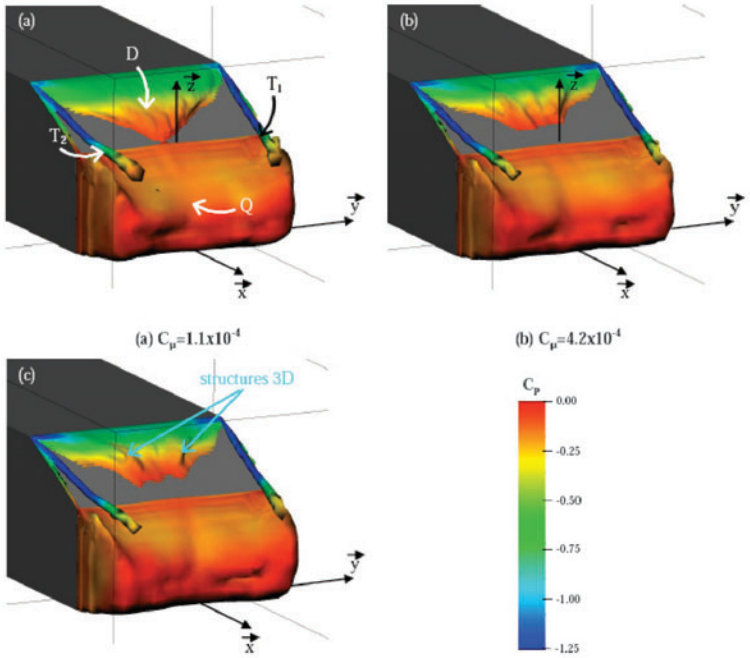

Figure 13. Pressure coefficient

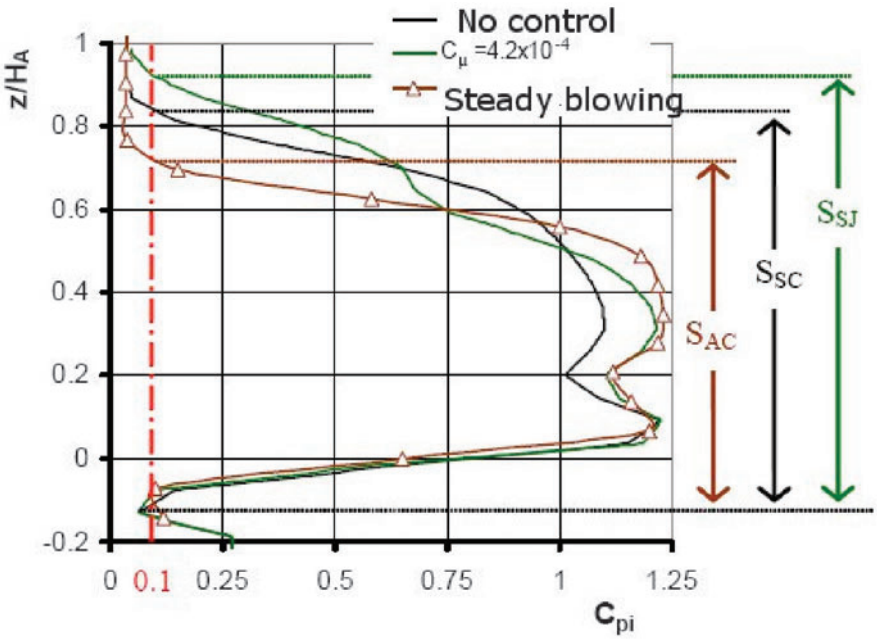

Figure 14. Total pressure coefficient evolution

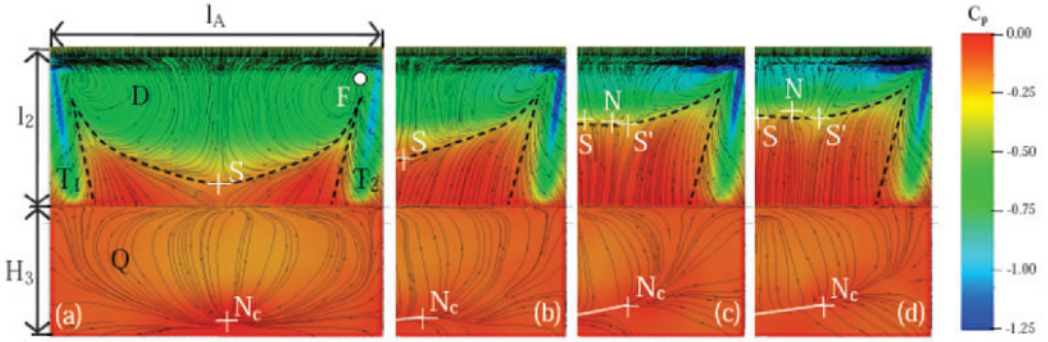

Figure 15. Visualization of surface streaklines

III.2.2.b-Effect of slot position

Two positions have been tested upstream (-10^{-3} m) and downstream (10^{-3} m) from the top of the rear window. In both cases the velocity was normal to the wall. The width of the slot is equal to 0.5×10^{-3} m and its span is 95% of the total rear window. The Reynolds number is also constant Re $=2.8\times10^{6}$ (U_0=40 m/s). Computations have been done for the three momentum coefficients (C_μ). For sake of clarity, we only report, in this paper, the results obtained in the case of the higher drag reduction, i.e. for $C_\mu=4.2\times10^{-4}$. However, for both slot positions, the evolution function of momentum coefficient is equivalent. The maximum drag reduction is equal to 5.2% and 13% respectively for the upstream and downstream actuators.

The iso-surface of the energy loss for the two positions is plotted in figure (16). One can see that the energy loss distribution is smoother in the case of the downstream actuator than in the case of the upstream actuator. This suggests that the flow modified by the downstream actuator less departs from 2D. It can be also observed that the ends of the longitudinal vortices are larger in the case of the upstream actuator. The comparison in the median plane shows that the separated bubble is shorter with the downstream actuator (figure 17). Therefore, the downstream control promotes more homogeneous, 2D and less energetic losses in comparison with the upstream control.

The profiles of the static pressure coefficient C_p, obtained downstream from the geometry in the case of the downstream actuation, are plotted on figure 18, for various momentum coefficients. For comparison, the results obtained without control have been added on this graph. Note that the shape of the profiles seems independent of the value of C_μ. At the top of the rear window, the values of C_p are lower than –1.2. It is worth noticing that, for the downstream actuation, this value spans the entire rear window whereas it is only the case near the lateral edges for the upstream control. The important low pressure zone induced by the synthetic jet is then followed by a high pressure zone. In the bubble separation zone, C_p is approximately equal to –0.5 with upstream control and –1 in the downstream one. Unlike the reference case, one can see that C_p decreases along the rear window, confirming therefore that the flow is globally attached along the rear window in the case of the downstream control. At the base the evolution of C_p is approximately the same for the two positions, slightly lower with the downstream one.

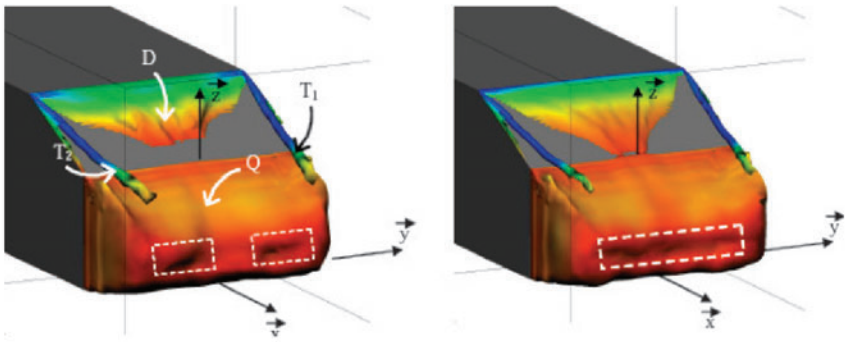

Figure 16. Pressure coefficient distribution (left actuator before the top of rear window, actuator after)

We remind that for the previous 2D computation, at the base, C_p increases. For the 3D computation, an increase is also obtained but with lower values.

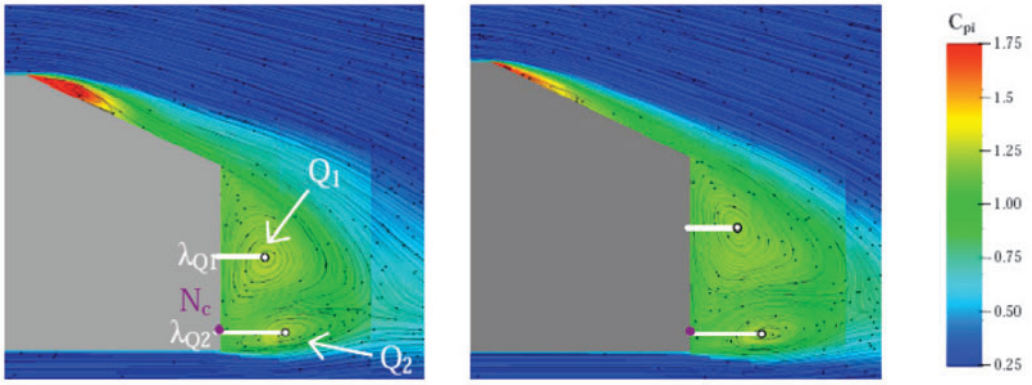

Figure 17. Total pressure coefficient distribution, (C_μ=4.2×10^{-4}, F_w^+=0.7) (left actuator before the top of rear window, actuator after)

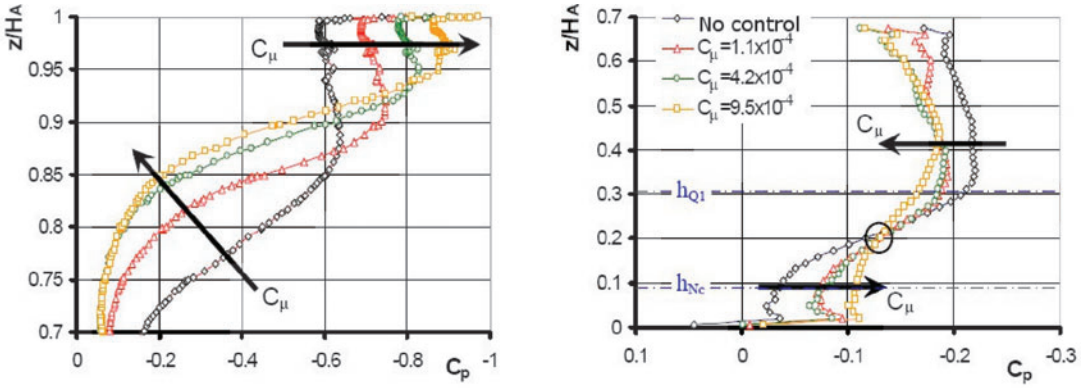

Figure 18. Static pressure coefficient distribution at the center plane (left : at the rear window, right : at the base)

IV. CONCLUSIONS

An extensive numerical parametric analysis, based on the Lattice-Boltzmann method, has been conducted on a simplified Ahmed body type geometry in order to investigate and develop a wake flow control technique by means of a synthetic jet. Using this system, implemented in an open-loop strategy, the aerodynamic drag has been reduced.

Preliminary 2D computations have been done to evaluate the influences of both the momentum coefficient and the reduced frequency of the synthetic jet have been investigated in details, at a fixed orifice position and width. The synthetic jet, placed upstream from the natural flow separation on the upper part of the rear window, is used to modify the distribution of static pressures applying over the entire rear part of the geometry. Such modifications relate with a change to the topology of the wake of the geometry. The optimum drag reductions are reported for a reduced frequency of F+=0.7. At this frequency, the synthetic jet creates a significant localized depression on the upper part of the rear window associated with a continuous recompression, which is in turn accompanied by a significant pressure increase applied to the base. The topology of the flow in the wake evolves and the aerodynamic drag diminishes by 28%.

In the 3D configuration, the uncontrolled flow has been compared with success with previous experimental and numerical results on identical geometry. The synthetic jet effect has been analyzed by characterising both the mean flow and the unsteadiness. This has been emphasized by a spectral analysis highlighting the flow dynamics. A careful parametric investigation has permitted to determine the optimal reduced frequency, momentum coefficient and actuator position in terms of drag reduction. In the 3D case, until 13% drag reduction has been obtained. This reduction is higher than all those

obtained with other actuators (8 to 10 % drag reduction has been reached). The drag reduction is particularly related to a modification of the mean flow wake topology than to a specific use of the synthetic jet actuator. However, the use of the synthetic jet can be promoted due to its low energy supply in comparison to a continuous or pulsed jet.

V. ACKNOWLEDGMENTS

The authors acknowledge Dr. Q. Gallas for his relevant point of view about synthetic jet actuator, Dr. E. Levallois, Dr P. Gilliéron for their help and Dr N. Mazellier for writing improvement.

REFERENCES

[1] Hucho W.H**.**, 1998, Aerodynamics of road vehicle-*Ann. Rev. Fluid Mech.* **25**, pp. 485-537

[2] Ahmed S.R., Ramm R.& Falting G., 1984, Some salient features of the time averaged ground vehicle wake, *SAE technical paper series 840300*, Detroit 1984

[3] Gad-El-Hak M., 1996, Modern developments in flow control, *Applied Mechanics reviews,* **9**, pp. 365-379.

[4] Gad-El-Hak M, Pollard A, Bonnet J, editors. 1998, *Flow control: fundamentals and practices*, Berlin: Springer.

[5] Collis, S.S., Joslin R.D., Seifert A., Theofilis V., 2004, Issues in active flow control: theory, control, simulation, and experiment, *Progress in Aerospace Sciences*, 40, 237-289.

[6] Bewley T., Liu S., 1998, Optimal and robust control and estimation of linear paths to transition. *J Fluid Mech.*, 365:305–49.

[7] Cathalifaud P, Luchini, P., 2002, Optimal control by blowing and suction at the wall of algebraically growing boundary layer disturbances. In: Saric W, Fasel H, editors. *Proceedings of the IUTAM laminar-turbulent symposium,* V. Sedona, AZ, USA, p. 307–12.

[8] Seifert A., Bachat T., Koss D., Shepshelovich M. & Wygnanski I., "Oscillatory blowing: Atool to delay boundary-layer separation", *AIAA Journal*, Vol. 31, No.11, pp.2052-2060, 1993.

[9] Glezer A. and Amitay M., 2002, Synthetic jets, *Annu. Rev. Fluid Mech.* **34**, 503.

[10] Kourta A. and Vitale E., 2008, Analysis and control of cavity flow, *Phys. Fluids* **20**, 077104.

[11] Gilliéron P., 2002, Contrôle des écoulements appliqués à l'automobile. Etat de l'art, *Mécanique & Industries* 3, pp 515-524

[12] Bourgois S & Tensi J., 2003, Contrôle de l'écoulement par autour d'un cylindre par techniques fluidiques et acoustiques, *16eme Congrès Français de Mécanique, Nice*.

[13] Fournier G., Bourgois S., Pellerin S, Ta Phuoc L, Tensi J. & El Jabi,R., 2004, Wall suction influence on the flow around a cylinder in laminar wake configuration by Large Eddy Simulation and experimental approaches, *39e Colloque d'Aérodynamique Appliquée, Contrôle des écoulements,* 22-24 Mars, Paris.

[14] Rouméas M., Gilliéron P. & Kourta A., 2005, Réduction de traînée par contrôle des décollements autour d'une géométrie simplifiée: Etude paramétrique 2D, *17ème Congrès Français de Mécanique,* 29 Août au 02 Septembre 2005, Troyes

[15] Onorato M., Costelli A.F. & Garonne A., 1984, Drag measurement through wake analysis, *SAE, SP-569, International congress and Exposition,* Detroit 1984

[16] Spohn A. & Gilliéron P., 2002 Flow Separations Generated by a Simplified Geometry of an Automotive Vehicle, *Congrès IUTAM Symposium on Unsteady Separated Flows, April 8-12, 2002, Toulouse, France*

[17] Beaudoin J.F, Cadot O., Aider J.L., Gosse K., Paranthoën P., Hamelin B., 2004**,** Cavitation as a complementary tool for automotive aerodynamics, *Experiments in Fluids*, **37** pp. 763-768

[18] Rouméas M., Gilliéron P. & Kourta A., 2008, Separated flows around the rear window of a simplified car geometry, *Journal of Fluid Engineering,* vol. **130** /021101-1

[19] Rouméas, M., Contribution à l'analyse et au contrôle du sillage épais par aspiration ou soufflage continu, PHD Thesis, *Thèse de Doctorat, INP Toulouse,* 2006.

[20] Gilliéron P. & Kourta A., Aerodynamic drag reduction by vertical splitter plates, Experiments in Fluids, **48**(1), pp. 1-16, 2010, DOI: 10.1007/s00348009-0705-7.

[21] Pujals G., Depardon S., Cossu C., Drag reduction of a 3D bluff body using coherent streamwise Streaks, *Exp Fluids* (2010) 49:1085–1094 DOI 10.1007/s00348-010-0857-5

[22] Fourié G., Keirsbulck L, P. Gilliéron , L. Labraga, Bluff-body drag reduction using a deflector, Exp Fluids (2011) 50:385–395 DOI 10.1007/s00348-0100937-6

[23] Bruneau CH, Mortazavi I (2008) Numerical modelling and passive flow control using porous media. *Comput Fluids* 37(5):488–498

[24] Boucinha V., Weber R., Kourta A., Drag reduction of a 3D bluff body using plasma actuators, *Int. J. Aerodynamics*, Vol. 1, Nos. 3/4, pp 262-281, 2011.

[25] Aubrun S., Alvi F., Kourta A., Separation flow control on a generic ground vehicle using steady microjet arrays, *AIAA conference, 5th Flow control conference*, 28 June-1 July 2010, Chicago, USA.

[26] Aubrun S., Alvi F., Leroy A., Kourta A., Active flow control of the 3D separation on Ahmed body using steady microjet arrays, *Proceedings of the 3rd Joint US-European Fluids Engineering Summer Meeting FEDSM2010*, August 1-5, 2010, Montreal, Canada.

[27] Pastoor M, Henning L, Noack BR, King R, Tadmor G (2008) Feedback shear layer control for bluff body drag reduction. *J Fluid Mech* 608:161–196

[28] Bideaux E., Bobiller P., Fournier E., Gilliéron P., Gilotte P., El Hajem M., Champagne J.Y., Kourta A., Drag reduction by pulsed jets on strongly unstructured wake: towards the square back control, *Int. J. Aerodynamics*, Vol. 1, Nos. 3/4, pp 282-298, 2011.

[29] Krajnović, S. and Fernandes J., Numerical Simulation of the Flow Around a Simplified Vehicle Model with Active Flow Control, *International Journal of Heat and Fluid Flow*, doi:10.1016/j.ijheatfluidflow.2010.06.007

[30] Brunn A, Wassen E, Sperber D, Nitsche W, Thiele F (2007) Active drag control for a generic car model. Notes Numer Fluid Mech Multidiscip Design 95:247–259

[31] Eichinger S., Tiele F., Wassen E., LES of active separation control on bluff bodies by steady blowing, *Proceedings of ASME 2010 3rd Joint US, European Fluids Engineering Summer Meeting and 8th International Conference on Nanochannels, Microchannels, and Minichannels*, FEDSM2010-ICNMM2010, August 2-4, 2010, Montreal, Quebec, Canada

[32] Kotapati R.B., Mittal R., Cattafesta III L.N., Numerical study of a transitional synthetic jet in quiescent external flow, *J. Fluid Mech.* (2007), vol. 581, pp. 287–321.

[33] Jain M., Puranik B., Agrawal A., A numerical investigation of effects of cavity and orifice parameters on the characteristics of a synthetic jet flow, *Sensors and Actuators* A 165 (2011) 351–366

[34] Rouméas M., Gilliéron P. & Kourta A, Drag reduction by flow separation control on a car after body, *Int. J. Numer. Meth. Fluids* (2008) DOI: 10.1002/fld.1930

[35] Chen S., Chen H. , Martinez D. & Matthaeus W., 1991, Lattice Boltzmann Model for simulation of magnetohydrodynamics, *Phys. Rev. Lett.*, **67**, pp 3776-3779.

[36] Rouméas M., Gilliéron P. & Kourta A., 2008, Analysis and control of the near–wake flow over a square-back geometry, *Computers and Fluids*, **38**, 2009, pp. 60-70, doi:10.1016/j.compfluid.2008.01.009.

[37] Chen S., Chen H. & Matthaeus W., 1992, Recovery of the Navier-Stokes equations using a lattice-gas Boltzmann method, *Phys. Rev. Ann.*, **45**, R5339-42

[38] Bhatnagar P.L., Gross E.P. & Krook M., 1954, A model for collision processes in gases. Small amplitude processes in charged and neutral one-component systems. *Phys. Rev.*, **94**(3), pp 511-525.

[39] Chen H., Teixeira C. & Molvig K., 1997, Digital Physics approach to computational fluid dynamics: some basic theoretical features, *Int. J. Modern Phys. C*, 8(4), pp. 675-684.

[40] Yakhot V. & Orszag S.A., 1986, Renormalization group analysis of turbulence. Basic theory. *Int J. Sci. Comput,* 1, pp. 1-51

[41] Pervaiz M. & Teixeira M., 1999, Two equation turbulence modeling with the lattice-Boltzmann method, *proceedings of ASME PVP Division conference, 2nd International Symposium on Computational Technologies for Fluid/Thermal& Chemical systems with industrial applications, Boston.*

[42] Gilliéron P. and Chometon F.; *Modelling of stationary three-dimensional detached airflows around an Ahmed Reference Body,* Third International Workshop on Vortex, ESAIM, Proceedings, Vol 7, 1999, pp 173-182, http://www.emath.fr/proc/Vol7/.

[43] Lehugeur B., Gilliéron P. & Ivanic T., 2006, Contribution de l'éclatement tourbillonnaire à la réduction de la traînée des véhicules automobiles: approche numérique, C.R. Mécanique 334 pp. 368-372.

[44] Krajnovic S. and Davidson L., 2005, Flow around a simplified car, part 1: Large Eddy Simulation, *Journal of Fluid Engineering*, 2005, 127, 907-918.

[45] Krajnovic S. and Davidson L., 2005, Flow around a simplified car, part 2: Understanding the flow, *Journal of Fluid Engineering*, 2005, 127, 919-928.

[46] Conan B., Antoine J., Planquart P., Experimental aerodynamic study on a car-type bluff body, 2011, *Exp. Fluids*, 50:1273-1284.

[47] Lienhart H., Stoots C. & Becker S., "Flow and turbulence structures in the wake of a simplified car model (Ahmed model)", roc. DGLR Fach. Symp. Der AG STAB, Stuttgart, 2002.

[48] Leclerc, C., Réduction de la traînée d'un véhicule automobile simplifié à l'aide du contrôle actif par jet synthétique, PHD Thesis, *Thèse de Doctorat, INP Toulouse,* 2008.

[49] Vino G., Watkins S., Mousley P., Watmuff J. & Prasad S., "Flow structures in the near-wake of the Ahmed model", *Journal of Fluids and Structures*, No. 20, pp. 673-695, 2005.

[50] Serre E., Manguez M., Pasquitté R., Guilmineau E., Deng G.B., Kornhass M., Shäfer M., Fröhlich J., Hinterberger C., Rodi W., On simulating the turbulent flow around the Ahmed body: French-German collaborative evolution of LES and DES, Computers & Fluids (2011), doi: 10.1016/j.compfluid.2011.O5.017

[51] Boucinha V., Weber R., Kourta A., Drag reduction of a 3D bluff body using plasma actuators, *Int. J. Aerodynamics*, Vol. 1, Nos. 3/4, pp 262-281, 2011.

[52] Minguez M., Pasquetti R., Serre E., High-order large-eddy simulation of flow over the "Ahmed body" car model, *Physics of Fluids* 20, 095101, 2008.